PHOTONICS Research

Topologically protecting squeezed light on a photonic chip

Ruo-Jing Ren,[1,2] Yong-Heng Lu,[1,2] Ze-Kun Jiang,[1,2] Jun Gao,[1,2] Wen-Hao Zhou,[1,2] Yao Wang,[1,2] Zhi-Qiang Jiao,[1,2] Xiao-Wei Wang,[1,2] Alexander S. Solntsev,[3] and Xian-Min Jin[1,2,4,*]

[1]Center for Integrated Quantum Information Technologies (IQIT), School of Physics and Astronomy and State Key Laboratory of Advanced Optical Communication Systems and Networks, Shanghai Jiao Tong University, Shanghai 200240, China
[2]CAS Center for Excellence and Synergetic Innovation Center in Quantum Information and Quantum Physics, University of Science and Technology of China, Hefei 230026, China
[3]School of Mathematical and Physical Sciences, University of Technology Sydney, Ultimo, New South Wales 2007, Australia
[4]TuringQ Co., Ltd., Shanghai 200240, China
*Corresponding author: xianmin.jin@sjtu.edu.cn

Received 12 October 2021; accepted 27 November 2021; posted 30 November 2021 (Doc. ID 445728); published 24 January 2022

Squeezed light is a critical resource in quantum sensing and information processing. Due to the inherently weak optical nonlinearity and limited interaction volume, considerable pump power is typically needed to obtain efficient interactions to generate squeezed light in bulk crystals. Integrated photonics offers an elegant way to increase the nonlinearity by confining light strictly inside the waveguide. For the construction of large-scale quantum systems performing many-photon operations, it is essential to integrate various functional modules on a chip. However, fabrication imperfections and transmission cross talk may add unwanted diffraction and coupling to other photonic elements, reducing the quality of squeezing. Here, by introducing the topological phase, we experimentally demonstrate the topologically protected nonlinear process of four-wave mixing, enabling the generation of squeezed light on a silica chip. We measure the cross-correlations at different evolution distances for various topological sites and verify the nonclassical features with high fidelity. The squeezing parameters are measured to certify the protection of cavity-free, strongly squeezed states. The demonstration of topological protection for squeezed light on a chip brings new opportunities for quantum integrated photonics, opening novel approaches for the design of advanced multi-photon circuits.

https://doi.org/10.1364/PRJ.445728

1. INTRODUCTION

Over the last few decades, researchers have witnessed the emerging field of quantum information [1]. Various advances have been achieved in a plethora of hardware platforms [2,3]. A photon, due to its fast speed and robustness with respect to the thermal environment, is considered a perfect information carrier for quantum information processing [4,5]. Thus, nonclassical light sources, particularly indistinguishable correlated photon pairs, are a key resource for quantum communication [6,7] and quantum computation [8–11]. Besides these advances focusing on Fock-like states, squeezed light also serves as another fundamental resource for quantum information [12–15]. Parametric frequency conversion in nonlinear crystals is an indispensable approach in quantum optics to obtain nonclassical light [16,17], as well as to generate multi-photon entangled states [18–21].

To obtain efficient nonlinear interactions in bulk crystals, tight focusing is required. That, however, leads to small Rayleigh length, limiting the interaction volume. An alternative approach of using high pump powers may lead to undesired effects, including photorefraction and damage to the material. In the last few years, integrated photonics has stood out by offering a compact solution in the form of optical waveguides [22,23], which greatly reduces such undesirable effects by confining the pump light inside the waveguide, offering both tight focusing and large interaction volume at the same time. Recent progress in this field includes waveguide-based quantum sources implemented by femtosecond laser writing [24], UV-laser writing [25], and silicon photonics [26,27]. These platforms feature excellent generated photon brightness, purity, and low propagation loss on a chip. Recent work has shown the potential for an integrated source to encode information in both discrete and continuous variables [28].

To construct large-scale photonic quantum systems, high-quality building blocks should be integrated in a compact footprint with considerable complexity [29]. Compared to the silicon photonics platform, femtosecond laser writing chips show the capability of fully three-dimensional integration, which is suitable for efficient simulation of two-dimensional

structures [30,31], and can be used to carry out various quantum information processing tasks [32–34]. When a nonclassical light source module is embedded into a complex on-chip arrangement, unwanted cross talk is prone to occur between adjacent waveguides due to the evanescent coupling. This cross talk not only modifies the generated quantum states of light, but also decreases the generation efficiency, since the pump light diverges into neighboring sites. The nonclassical features of the generated photons, for example, the photon-pair cross-correlations and the squeezing quality, can also decay because of this unwanted coupling. The key challenge is to protect efficient use of nonlinearity and quantumness of the generated photon pairs.

The topological phase allows protection of physical fields against unavoidable disorder. This effect was at the heart of recent demonstrations of topological protection for various nonlinear optical processes [35,36], including photon-pair generation [37–42]. The above, however, was studied only in the regime of low photon numbers, while strongly squeezed light remained out of scope despite the significant importance of squeezing in quantum optics. In this paper, we experimentally demonstrate the topological protection of squeezed light with a dimerized-type chain resembling Su–Schrieffer–Heeger (SSH) lattices on a photonic chip. We observe robust localization of topological states at different wavelengths. We verify the topological protection of quantum resources by measuring the transport dynamics such as light field distributions, cross-correlations, and squeezing by switching incident pump light between different input ports. Our results demonstrate that the topological protection is robust to the change in wavelength of nonclassical states, and can help to construct quantum squeezers in complex photonic circuits tolerant to fabrication imperfections.

2. EXPERIMENTS

Our topologically protected lattices are inscribed in a 20 mm × 35 mm × 1 mm fused silica block by femtosecond laser direct writing. The writing laser has a wavelength of 513 nm and a repetition rate of 1 MHz. Based on our previous work [28], the waveguide itself can function as a four-wave-mixing (FWM) source, following energy and momentum conservation, $2\hbar\omega_p = \hbar\omega_s + \hbar\omega_i$ and $2\hbar k_p = \hbar k_s + \hbar k_i$, where ω stands for frequency, k stands for wave vectors, and indices p, s, and i correspond to pump, signal, and idler waves, respectively. In this process, glass absorbs two photons from the pump wave, and generates signal and idler photon pairs, where the birefringence induced phase matching condition is fulfilled as

$$\Delta k = \frac{2[n(\omega_p) + \Delta n]\omega_p}{c} - \frac{n(\omega_s)\omega_s}{c} - \frac{n(\omega_i)\omega_i}{c} = 0. \quad (1)$$

Here, n stands for refractive index, c is the speed of light, and birefringence Δn fulfills the phase-matching condition.

The lattices for the topological protection of quantum light are composed of coupled waveguides with two sets of spacings, corresponding to the modulation of alternating couplings J_1 and J_2, which can be described by the following Hamiltonian:

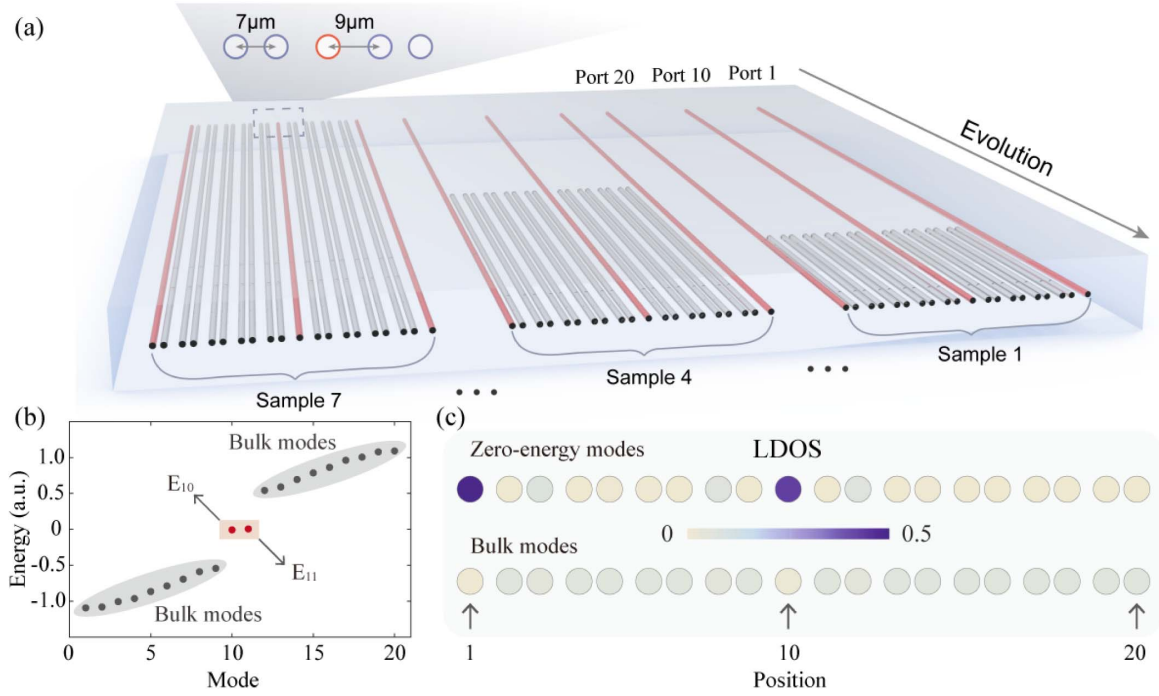

Fig. 1. Schematic diagram of the lattice with topological protection for squeezed light. (a) The structure of the lattice contains seven groups with lattice distances ranging from 5 mm to 35 mm. The short and long separations between adjacent waveguides are 7 μm and 9 μm, respectively. (b) Spectrum of the lattice. There are only two quasi zero-energy modes E_{10} and E_{11} and two extended bulk bands. Modes E_{10} and E_{11} are located inside the bandgap and decouple from the bulk bands, which promotes topological protection. a.u., arbitrary units. (c) Spatial distribution with combined local density of states (LDOS) for the quasi zero-energy modes E_{10} and E_{11} (upper line) marked by red in (b) and bulk modes (bottom line) marked by gray in (b).

$$H = \sum_n (J_1 a_n^\dagger b_n + J_2 b_n^\dagger a_{n+1}) + \text{h.c.} \quad (2)$$

Terms $a_n^\dagger$ (a_{n+1}) and $b_n^\dagger$ (b_n) are the creation (annihilation) operators at corresponding sites with different spacings (see Appendix B for details of the SSH model). The lattices possess two topologically protected channels: the edge-state channel and the interface-defect channel, as shown in Fig. 1(a). Here, we set separation distances $l_1 = 7$ μm and $l_2 = 9$ μm, respectively. The dimerized-type chain resembling the SSH model [43] enables topological nontrivial phases with edge states described by the bulk-edge correspondence [44,45]. The edge states can be regarded as the topological transition interface between trivial vacuum and nontrivial lattice structure. In addition, the interface-defect channel in the middle of the lattice acts as a topologically protected interface state [46] by interfacing two versions of the dimerization patterns with distinct Zak phases [47,48], which is supported by the existence of the topological phase transition between them.

We further illustrate the band diagram by characterizing the spectrum of the lattice, as shown in the Fig. 1(b). The band diagram contains two extended bands separated by the bandgap. Inside the bandgap, there are two modes E_{10} and E_{11} pinning on the quasi zero-energy level and decoupled from the bulk band, which reveals the existence of topological edge states. The spatial distribution can be characterized by the eigenmode local density of states (LDOS) [49–51], which can be defined as $D_n(E) = \sum_m \delta(E - E_m)|\varphi_n^{(m)}|^2$, where E_m is the energy of the mth eigenstate with wave function $\varphi_n^{(m)}$, and n is the site label. As shown in Fig. 1(c), the combined LDOS of the two gapped zero-energy modes indicates that the modal amplitudes with maxima appear at ports 1 and 10, while the minima appear at other ports including port 20. In addition, in the bulk modes, there is no confinement in the chain. It shows localization in edge channel 1 and interface-defect channel 10 supported by the norm of topologically protected zero-energy modes. In contrast, the low amplitude at port 20 for all modes indicates that edge channel 20 is trivial, allowing photons to diffuse into the bulk of the lattice. Therefore, among the three input ports in the lattice used for squeezed light (depicted in Fig. 1), edge-state channel 1 and interface-defect channel 10 both are topologically protected, while edge channel 20 is not.

The experimental setup is schematically depicted in Fig. 2(a) (see Appendix F for experimental details). The mode-locked 780 nm femtosecond pump pulses (80 MHz) with vertical polarization (prepared by a combination of wave plates and a Glan–Taylor polarizer) can be injected into three different ports, namely, 1, 10, and 20. The output light intensity distributions of the pump light are accumulated by a CCD camera, and the evolution patterns under different distances varying from 5 mm to 35 mm [see I, II, and III in Fig. 2(b)] are also recorded. We experimentally verify the localization effect in the above three ports by comparing the measured pattern with theoretical simulation in Fig. 2(b). It is obvious that the pump light propagates locally as time evolves in the edge-state channel and the interface-defect channel (topological cases), while the beam diffuses and gradually couples to the adjacent sites in edge channel port 20 (trivial case). The localization effect in the topological channel ports indicates protection of the pump

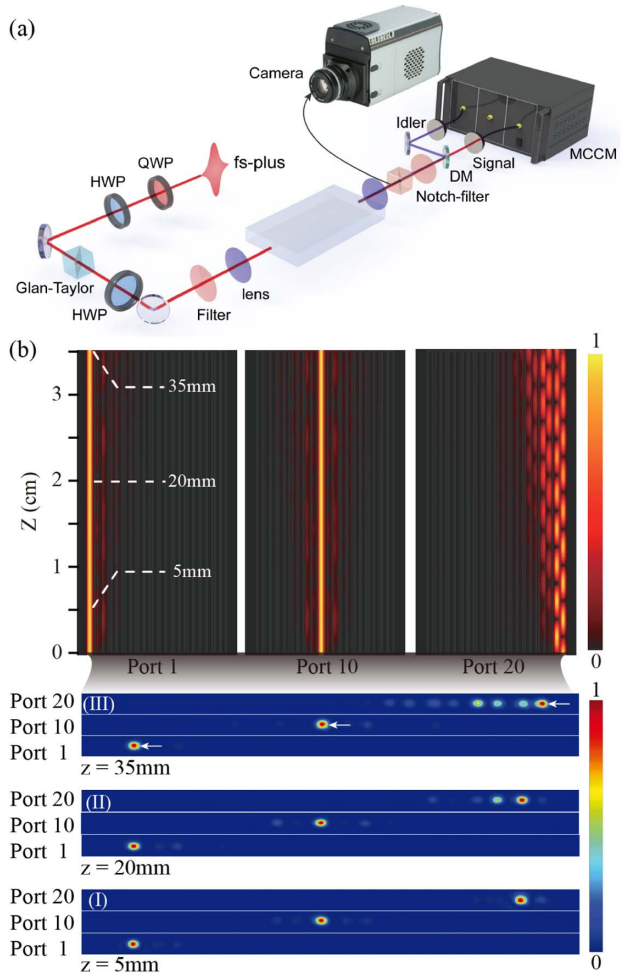

Fig. 2. Experimental setup and intensity distributions of pump light. (a) Experimental setup for generation, filtering, and evolution measurement of nonclassical light. The input ports can be switched. DM, dichroic mirror; MCCM, multi-channel coincidence module. (b) Simulated intensity distributions of the pump light from ports 1, 10, and 20. The evolution distance is marked in white. (I), (II), and (III) show the experimentally measured intensity distributions from three input channel ports at 5 mm, 20 mm, and 35 mm evolution distances, respectively. The protected states from ports 1 and 10 always maintain localization as the propagation distance increases, while the unprotected state from port 20 diffuses over the lattice. The intensity distribution is normalized to its maximum.

intensity, and provides sufficient power for generating photon pairs during FWM. The diffusion degrades the intensity as the propagation length increases, and the decreased pump intensity fails to achieve a high-quality quantum source during the FWM process. It can be deduced that the FWM in ports 1 and 10 is well protected at the wavelength of 780 nm. The pump light is spatially confined, and this localization makes FWM more efficient.

After verifying the spatial protection of the pump light, we further test whether the on-chip generated correlated photons can also be protected. We first calculate the light intensity distributions of the signal and idler photons, and the theoretical simulation results are presented in Figs. 3(a) and 3(b),

respectively. Even for light with different wavelengths, the localization effect still emerges in the topologically protected channels. To retrieve the signal and idler photons, we first filter out the residual pump light using both the polarization filter (Glan–Taylor polarizer) and spectrum filter (notch filters centered as 780 nm). Then, signal and idler photons are separated into two different spatial modes by a dichroic mirror, where idler photons are transmitted while signal photons are reflected. The photon pairs are coupled into single mode fibers, and then detected by avalanche photodiodes. All the coincidence counts are recorded by a homemade multi-channel coincidence module (MCCM). The experimental layout can be found in Fig. 2(a). To quantify the nonclassical features of the correlated photon pairs, we introduce the cross-correlation function as follows:

$$g_{si}^{(2)}(0) = \frac{\langle \hat{a}_s^\dagger \hat{a}_i^\dagger \hat{a}_i \hat{a}_s \rangle}{\langle \hat{a}_s^\dagger \hat{a}_s \rangle \langle \hat{a}_i^\dagger \hat{a}_i \rangle}. \tag{3}$$

In the FWM case, a value higher than two of the cross-correlation function $g_{si}^{(2)}(0)$ is evidence of nonclassical light, although, for instance, the violation of the Bell inequality requires $g_{si}^{(2)}(0)$ larger than six [52].

The cross-correlations $g_{si}^{(2)}(0)$ are measured for the pump power of 1 mW with integration time of 50 s. The cross-correlations $g_{si}^{(2)}(0)$ in edge-state port 1 vary from 50.03 ± 3.85 to 89.34 ± 9.53 with evolution distances from 5 mm to 35 mm, which is strong evidence of nonclassical light. The cross-correlations $g_{si}^{(2)}(0)$ in interface-defect port 10 vary from 49.01 ± 2.75 to 99.25 ± 10.07, indicating the protection of the photon pair generation process. For the same transport length, in contrast, the maximum cross-correlation $g_{si}^{(2)}(0)$ from unprotected edge port 20 reaches only a range of 10.58 ± 1.82 to 25.65 ± 5.6. As can be seen in Fig. 3(c), the topologically protected structure can provide nearly five times higher cross-correlation values than those in unprotected states. In the low pump regime, higher values of $g_{si}^{(2)}(0)$ indicate topological protection, which can help with losses and decoherence during transmission [53]. We also study the unheralded autocorrelation functions for signal and idler fields in the low-gain regime (pump power at 5 mW) for the multimode analysis (see Appendix D for details). The results indicate that our on-chip sources are broadband multimode squeezers.

Due to the strong confinement of the pump light, our source can function as a squeezed light source [54] in the high-power regime. The threshold for optical damage, photorefraction, and other unwanted effects for fused silica is very high; thus, combined with the lattices for topological protection, both weak pump and strong pump regimes can be implemented. In the strong pump regime, the high-order terms of the photon-pair generation process are dominant, leading to the generation of squeezed light. In this work, we compare the squeezing parameters among three different structures. Squeezing parameter λ can be calculated by measuring the autocorrelation function $g_H^{(2)}(0)$ and heralding efficiency η_H using the following formula (see Appendix A for details of the formula and the fluctuation analysis) [25]:

$$\lambda^2 = g_H^{(2)}(0) \frac{\eta_H}{2[1-(1-\eta_H)^2]}. \tag{4}$$

As shown in Fig. 4, the squeezing parameters for the three channels are depicted in different colors under different evolution distances, where two distinct features can be observed. In the long evolution distance regimes, the squeezing parameters of the topologically protected channels are larger than that of

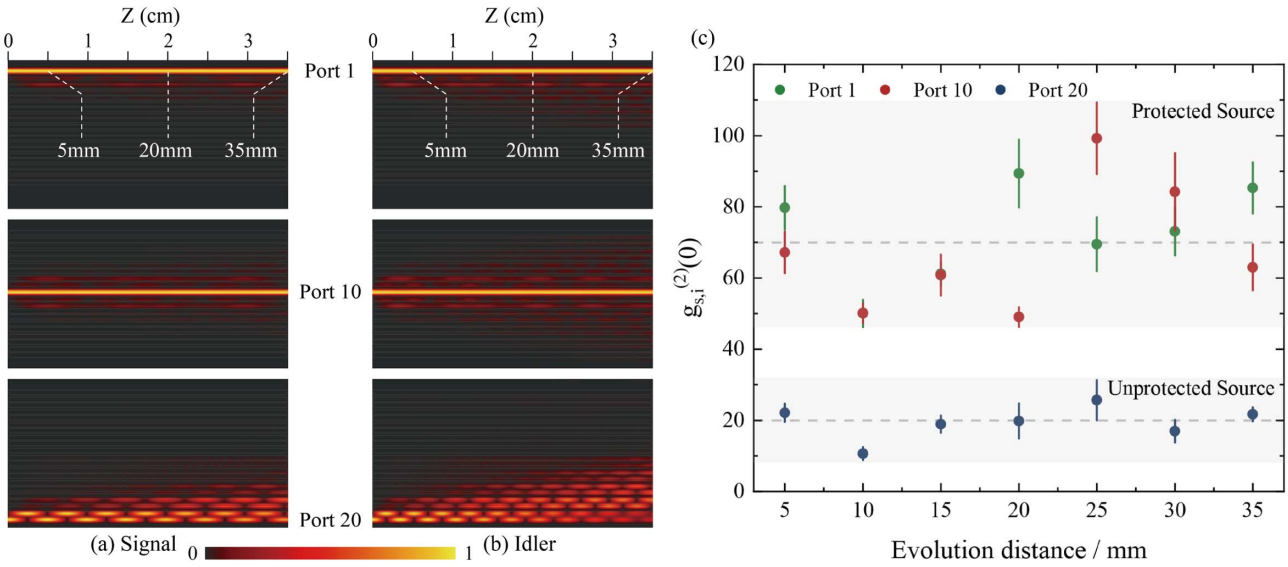

Fig. 3. Performance of topological protection for the generated photon pairs. (a) Evolution of the signal photons generated with pump in different input ports. (b) Evolution of the idler photons generated with pump in different input ports. (c) Cross-correlations $g_{si}^2(0)$ with different input ports 1, 10, and 20 at different propagation distances from 5 mm to 35 mm with a step of 5 mm. The pump power is 1 mW with the integration time of 50 s. Cross-correlations $g_{si}^2(0)$ of channel ports 1 and 10 are depicted in green and red, respectively, with high values, which demonstrates the topological protection of FWM. Cross-correlation $g_{si}^2(0)$ in port 20 is depicted in blue, with the corresponding values being five times lower than the protected states from ports 1 and 10.

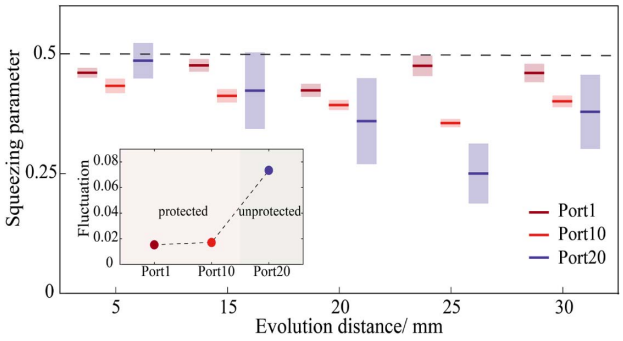

Fig. 4. Experimental verification of topological protection for squeezed light. The squeezing parameters in ports 1, 10, and 20 are depicted in deep red, red, and blue, accordingly. The values of the squeezing parameters are more uniform and higher in two protected cases compared with unprotected port 20. The variance among three topological channels is different since unprotected port 20 fluctuates in a wider range. The inset shows the average fluctuation from each port. Compared to the results of the other two channel ports, channel port 20 is unprotected.

the unprotected channels. In addition, the measured fluctuations using Possionian statistics in port 20 are greatly influenced by the beam diffusion unlike the topologically protected ports. These results indicate that the squeezed states can be well protected in the topological structure.

3. CONCLUSION

In conclusion, we have reported the topological protection of on-chip FWM and the generated squeezed light. By introducing a topological phase with a dimerized-type chain resembling SSH lattices on a silica photonic chip, we have observed localization and strong confinement of the pump light in topologically protected channels. The protected pump field fulfills the tight focusing condition to allow the waveguide to function as a high-quality quantum squeezer. We have demonstrated that the protection applies to different wavelengths, impacting the cross-correlations and squeezing parameters. It showcases a robust generation of quantum resources for future practical quantum information tasks, such as Gaussian boson sampling and bosonic error correction. We have verified the validity of the topological protection of on-chip squeezers, which may play an essential role in photonic quantum information processing (see Appendix C for discussions of robustness and validity) [55].

APPENDIX A: CALCULATION OF THE SQUEEZING PARAMETER

In this paper, we adopt the Oxford group's method to evaluate the squeezing parameter [25]. The two-mode squeezed vacuum state is defined as

$$|\psi_{\mathrm{TMSV}}\rangle = \hat{S}_0|0\rangle = \sqrt{1-\lambda^2}\sum_{n=0}^{\infty}\frac{(\lambda\hat{A}_0^{\dagger}\hat{B}_0^{\dagger})^n}{n!}|0\rangle. \tag{A1}$$

We measured the squeezing parameter λ by relating it to the heralded second-order correlation $g_H^2(0)$, which is regularly defined as

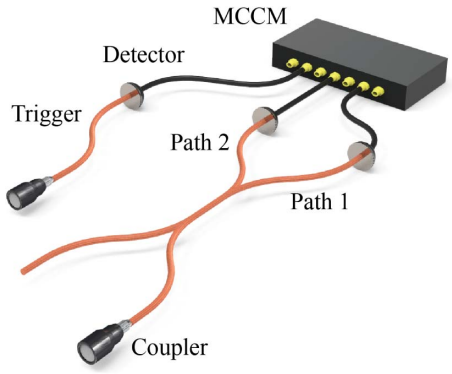

Fig. 5. Experimental schematic of measuring the heralded second-order correlation $g_H^{(2)}(0)$.

$$g_H^{(2)}(0) = \frac{N_{12t}N_t}{N_{1t}N_{2t}} = \frac{P_{12t}P_t}{P_{1t}P_{2t}}. \tag{A2}$$

As shown in Fig. 5, N_1 and N_2 are the photon counts of the heralded path split by a 50:50 beam splitter (BS). N_t is the heralding path acting as a trigger. Taking advantage of the MCCM, we can measure the coincidences between the desired channels. N_{1t}, N_{2t}, and N_{12t} are coincidence counts of the corresponding channels. P is the probability of observing coincident events in the subscripted modes.

The heralding efficiency η_H is calculated by

$$\eta_H = \frac{N_{1t}+N_{2t}}{N_t} = \frac{N_{\mathrm{si}}}{N_s}. \tag{A3}$$

As can be inferred from Eqs. (2) and (3), only when the higher order emission occurs will channels 1 and 2 and the trigger fire simultaneously. Then the probability of detecting these photons in channels 1 and 2 is $\eta_1\eta_2$. The corresponding probability that at least one of the two photons is not lost is $1-(1-\eta_H)^2$. Thus, we have

$$P_{12t} = \lambda^4[1-(1-\eta_H)^2]\eta_1\eta_2/2. \tag{A4}$$

We can obtain other terms in a similar way. Then we multiply these terms together and finally obtain the squeezing parameter:

$$\lambda^2 = g_H^{(2)}(0)\frac{\eta_H}{2[1-(1-\eta_H)^2]}. \tag{A5}$$

Regarding the fluctuation in Fig. 4, the values are calculated by the following error transfer formula:

$$\frac{1}{2}\lambda\sqrt{\frac{1}{N_{1t}}+\frac{1}{N_{2t}}+\frac{1}{N_{12t}}+\frac{1}{N_t}}. \tag{A6}$$

The fluctuation of the detected photon number is governed by Poisson statistics.

APPENDIX B: HAMILTONIAN OF TOPOLOGICALLY PROTECTED QUANTUM LIGHT LATTICES

As shown in Fig. 6, the topologically protected lattices for quantum light are composed of 20-site dimer chains with alternate large and small spacings. In the waveguide system, the

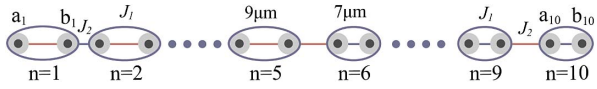

Fig. 6. Sketch of lattices for topological protection of squeezed light. There are 20 sites and 10 unit cells in the lattice. The red line marks the large spacing 9 μm with weak coupling of 0.3 mm^{-1}, while the blue line marks the small spacing 7 μm with strong coupling of 0.8 mm^{-1}.

coupling coefficient is determined by the spacing of adjacent waveguides [56]. Here, the large (small) spacing is 9 μm (7 μm), corresponding to the coupling coefficient of 0.3 mm^{-1} (0.8 mm^{-1}). Therefore, the photonic system can be described by the dimer Hamiltonian

$$H = \sum_n (J_1 a_n^\dagger b_n + J_2 b_n^\dagger a_{n+1}) + \text{h.c.}, \tag{B1}$$

where $J_1/J_2 = 0.375$ when $n \le 5$, and $J_1/J_2 = 2.67$ when $6 \le n \le 10$. The unit cell in the lattice consists of two sites labeled as a and b (see Fig. 2). Terms $a_n^\dagger\,(a_{n+1})$ and $b_n^\dagger\,(b_n)$ are the creation (annihilation) operators of two sites in the unit cell labeled as n. Parameters J_1 and J_2 represent the intracell and intercell coupling strengths, respectively. In addition, there is a large-spacing defect between unit cell 5 and unit cell 6, which resembles a so-called long-long defect[46].

APPENDIX C: ROBUSTNESS AND VALIDITY OF TOPOLOGICAL MODULES

In this section, we explain the motivation for topologically protected quantum light sources. Our work realizes the protection of squeezed light by a topological lattice. It is applicable to large-scale photonic structures where unwanted cross talk can pose a significant problem. Our method for protecting squeezed light may be practical in the following future scenarios.

1. Integrated photonics is now an emerging and promising platform for photonic quantum computing. Large-scale integration requires compact photonic device alignments. Photons, which are expected to be confined in a certain device, may diffuse into nearby photonic circuits on the same chip due to the inevitable evanescent coupling. In that case, our method can isolate quantum resources well against such diffusion loss by appropriate layouts.
2. In analog photonic computing, the Hamiltonian of a quantum system can be designed and engineered via geometric design. Our protocol offers an additional degree of freedom for the problem of Hamiltonian engineering by lifting many geometric limitations.

To further verify the robustness and validity of our model, we design and simulate different topological modules to test the cross talk effect in a one-dimensional lattice. As shown in Figs. 7(a) and 7(b), modules that contain two different topologically protected modes (port 1 and port 10) are inserted into a one-dimensional lattice with uniform spacing. Modules containing port 1 have 4 waveguides, while modules containing port 10 have a seven-waveguide structure. As a comparison, the trivial scenario containing port 20 [Fig. 7(c)] is also considered.

The uniform-spacing lattices are chosen to have three different spacings, as Figs. 7(d)–7(f) show. It is obvious that the topological modules inserted in different lattices all possess the power to confine the pump light in the injected port. Also see that the modules contain only a small number of waveguides, and such a structure is very compact. The performance verifies the robustness and validity of the topological modules to function as an independent unit to alleviate the cross talk problem. Such a degree of freedom for engineering Hamiltonians can be helpful for complex photonic integration design.

APPENDIX D: MULTI-MODE ANALYSIS OF FWM PROCESS

We can calculate the source joint spectral amplitude (JSA) using the following expression:

$$F(\omega_s, \omega_i) = N \int_0^L \mathrm{d}z \int \mathrm{d}\omega_p \alpha_p(\omega_p - \omega_p^0) \times \alpha_p(\omega_s + \omega_i - \omega_p - \omega_p^0) \exp(-\mathrm{i}\Delta k z). \tag{D1}$$

Here, N is a normalization coefficient, α_p is the pump envelope amplitude, L is the length of the waveguide, ω_p^0 is the central frequency of the pump light, and Δk is the first-order Taylor series about the phase mismatch parameter.

Using Schmidt decomposition on the JSA, we can obtain

$$F(\omega_s, \omega_i) = \Sigma_k \lambda_k \varphi_k(\omega_1) \varphi_k(\omega_2), \tag{D2}$$

where $\varphi_k(\omega_1)$ and $\varphi_k(\omega_2)$ are two orthogonal basis sets called the Schmidt modes. Cooperativity parameter K is then defined by

$$K = 1/\sum_k \lambda_k^4. \tag{D3}$$

Experimentally, we probe K by directly measuring the unheralded autocorrelation functions for signal and idler photons [53]:

$$g^{(2)}(0) = 1 + \frac{\sum_k \lambda_k^4}{(\sum_k \lambda_k^2)^2} = 1 + \sum_k \lambda_k^4 = 1 + \frac{1}{K}. \tag{D4}$$

In the low-gain regime (pump power is 5 mW), the measured results are 1.42 ± 0.08 and 1.77 ± 0.05, respectively. Thus, we can obtain $K_{\text{signal}} = 2.38$ and $K_{\text{idler}} = 1.3$. It is therefore confirmed that our on-chip sources are broadband multimode squeezers, which are regarded as powerful quantum resources.

APPENDIX E: ESTIMATION OF THE MODE FIELD DIAMETER

To estimate the mode field diameter of the fabricated waveguides, we extract the intensity distribution of each single light spot from the data collected by the CCD. One of the light spots is shown in Fig. 8(a) as an example. The intensity distribution is fitted by a 2D Gaussian function:

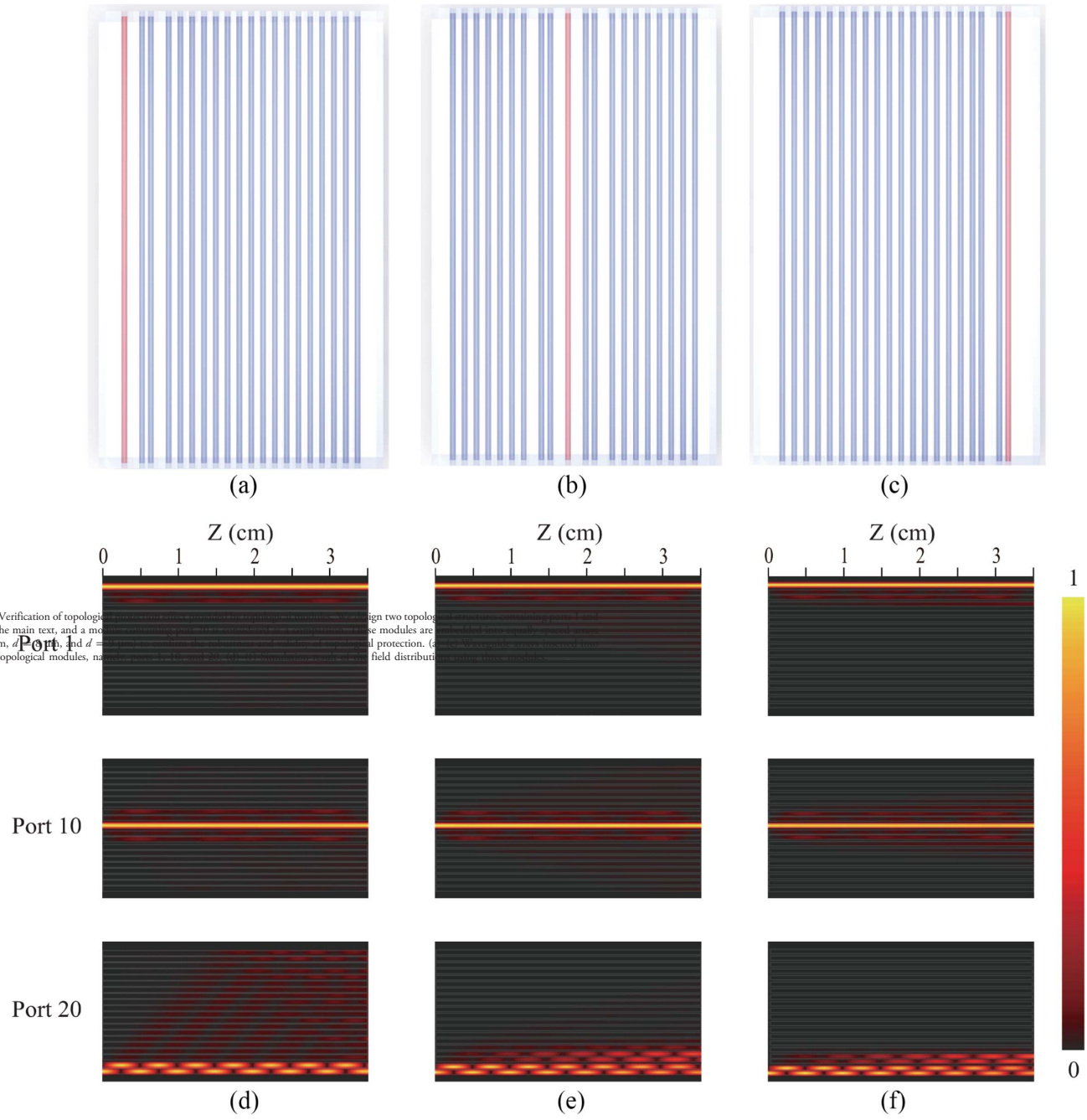

Fig. 7. Verification of topologi… ign two topolog… 10 from the main text, and a mo… se modules are … (d = 7 μm, d = … μm, and d = … al protection. (a… different topological modules, na… field distributi…

$$I = I_0 + A \exp\left[-\frac{1}{2}\left(\frac{x - x_c}{w_1}\right)^2 - \frac{1}{2}\left(\frac{y - y_c}{w_2}\right)^2\right]. \quad \textbf{(E1)}$$

Through fitting, we can calculate the pixel numbers of the horizontal and vertical field diameters at $1/e^2$ peak intensity points. The intensity profile after fitting is shown in the right part of Fig. 8. Then, we compare the pixel numbers between the adjacent waveguides with the real separations in the photonic chip. From this ratio, we can determine the scale of the CCD collected data and estimate the mode field diameter of the waveguides.

To reduce errors in the estimation process, we collect the intensity distribution of 18 light spots from three different groups, and calculate the average mode field diameter, which is (5.466 ± 0.389) μm in horizontal direction and (5.207 ± 0.217) μm in vertical direction.

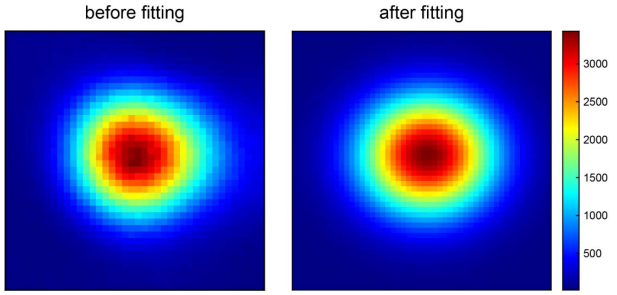

Fig. 8. Estimation of the mode field diameter. The intensity distributions of the light spots are extracted from the CCD data and fitted by 2D Gaussian functions. The beam diameters in x and y directions are calculated at the $1/e^2$ peak intensity points. We determine the scale of the figure by comparing the separation in pixel numbers and real waveguides. The final estimated results of horizontal and vertical field diameters are (5.466 ± 0.389) μm and (5.207 ± 0.217) μm, respectively.

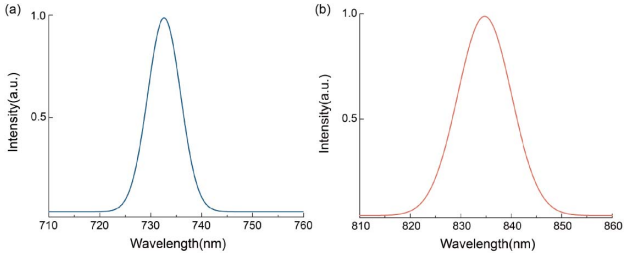

Fig. 9. Measured spectra of signal and idler photons.

APPENDIX F: EXPERIMENTAL DETAILS OF THE PHOTONIC CHIP AND THE MEASUREMENT SETUP

In our experiment, we use an ultrafast Ti:sapphire oscillator centered at 780 nm as the pump light. The generated signal and idler photon pairs are first separated by a dichroic mirror and three cascaded notch filters (Semrock, NF03-785E-25). Then, in both signal and idler photon arms, additional filters (Semrock, FF01-770/SP-25 and Semrock, BLP01-785R-25) are added to suppress the noise photons.

We also measure the spectra of both signal and idler photons, and the central wavelengths are 732.5 nm and 834.3 nm, respectively. The measured spectra are shown in Fig. 9. As can be inferred from Ref. [28], the fabrication accuracy is maintained in waveguide arrays as well. The perturbation of the birefringence is still within 5% for both idler and signal photons.

The collection efficiencies for the signal and idler photons into the optical fibers are almost the same, all beyond 85%. Through the subsequent on-chip filtering and further plans for "all on-chip project," we believe the coupling loss can be further decreased. However, in our current work, the relatively small photon losses do not have a strong impact on our results.

Funding. National Key R&D Program of China (2019YFA0308700, 2019YFA0706302, 2017YFA0303700); National Natural Science Foundation of China (NSFC) (11904229, 61734005, 11761141014, 11690033); Science and Technology Commission of Shanghai Municipality (STCSM) (20JC1416300, 2019SHZDZX01); Shanghai Municipal Education Commission (SMEC) (2017-01-07-00-02-E00049); China Postdoctoral Science Foundation (2020M671091); Australian Research Council (DE180100070); University of Technology Sydney Seed Fund.

Acknowledgment. X.-M.J. acknowledges additional support from a Shanghai talent program and support from Zhiyuan Innovative Research Center of Shanghai Jiao Tong University.

Disclosures. The authors declare no conflicts of interest.

Data Availability. Data underlying the results presented in this paper are not publicly available at this time but may be obtained from the authors upon reasonable request.

REFERENCES

1. M. Nielsen and I. Chuang, *Quantum Computation and Quantum Information* (Cambridge University, 2000).
2. T. D. Ladd, F. Jelezko, R. Laflamme, Y. Nakamura, C. Monroe, and J. L. O'Brien, "Quantum computers," Nature **464**, 45–53 (2010).
3. G. Popkin, "Quest for qubits," Science **354**, 1090–1093 (2016).
4. L. Mandel and E. Wolf, *Optical Coherence and Quantum Optics* (Cambridge University, 1995).
5. J. L. O'Brien, A. Furusawa, and J. Vučković, "Photonic quantum technologies," Nat. Photonics **3**, 687–695 (2009).
6. N. Gisin, G. Ribordy, W. Tittel, and H. Zbinden, "Quantum cryptography," Rev. Mod. Phys. **74**, 145–195 (2002).
7. F. Xu, X. Ma, Q. Zhang, H.-K. Lo, and J.-W. Pan, "Secure quantum key distribution with realistic devices," Rev. Mod. Phys. **92**, 025002 (2020).
8. C. K. Hong, Z. Y. Ou, and L. Mandel, "Measurement of subpicosecond time intervals between two photons by interference," Phys. Rev. Lett. **59**, 2044–2046 (1987).
9. P. Kok, W. J. Munro, K. Nemoto, T. C. Ralph, J. P. Dowling, and G. J. Milburn, "Linear optical quantum computing with photonic qubits," Rev. Mod. Phys. **79**, 135–174 (2007).
10. M. Lebugle, M. Gräfe, R. Heilmann, A. Perez-Leija, S. Nolte, and A. Szameit, "Experimental observation of N00N state Bloch oscillations," Nat. Commun. **6**, 8273 (2015).
11. C. Sparrow, E. Martín-López, N. Maraviglia, A. Neville, C. Harrold, J. Carolan, Y. N. Joglekar, T. Hashimoto, N. Matsuda, J. L. O'Brien, D. P. Tew, and A. Laing, "Simulating the vibrational quantum dynamics of molecules using photonics," Nature **557**, 660–667 (2018).
12. S. L. Braunstein and P. van Loock, "Quantum information with continuous variables," Rev. Mod. Phys. **77**, 513–577 (2005).
13. C. Weedbrook, S. Pirandola, R. García-Patrón, N. J. Cerf, T. C. Ralph, J. H. Shapiro, and S. Lloyd, "Gaussian quantum information," Rev. Mod. Phys. **84**, 621–669 (2012).
14. C. S. Hamilton, R. Kruse, L. Sansoni, S. Barkhofen, C. Silberhorn, and I. Jex, "Gaussian Boson sampling," Phys. Rev. Lett. **119**, 170501 (2017).
15. D. Gottesman, A. Kitaev, and J. Preskill, "Encoding a qubit in an oscillator," Phys. Rev. A **64**, 012310 (2001).
16. C. Kurtsiefer, M. Oberparleiter, and H. Weinfurter, "Generation of correlated photon pairs in type-II parametric down conversion-revisited," J. Mod. Opt. **48**, 1997–2007 (2001).
17. L. Caspani, C. Xiong, B. J. Eggleton, D. Bajoni, M. Liscidini, M. Galli, R. Morandotti, and D. J. Moss, "Integrated sources of photon quantum states based on nonlinear optics," Light Sci. Appl. **6**, e17100 (2017).
18. P. G. Kwiat, K. Mattle, H. Weinfurter, A. Zeilinger, A. V. Sergienko, and Y. Shih, "New high-intensity source of polarization-entangled photon pairs," Phys. Rev. Lett. **75**, 4337–4341 (1995).

19. J.-W. Pan, M. Daniell, S. Gasparoni, G. Weihs, and A. Zeilinger, "Experimental demonstration of four-photon entanglement and high-fidelity teleportation," Phys. Rev. Lett. **86**, 4435–4438 (2001).
20. X.-L. Wang, L.-K. Chen, W. Li, H.-L. Huang, C. Liu, C. Chen, Y.-H. Luo, Z.-E. Su, D. Wu, Z.-D. Li, H. Lu, Y. Hu, X. Jiang, C.-Z. Peng, L. Li, N.-L. Liu, Y.-A. Chen, C.-Y. Lu, and J.-W. Pan, "Experimental ten-photon entanglement," Phys. Rev. Lett. **117**, 210502 (2016).
21. H.-S. Zhong, Y. Li, W. Li, L.-C. Peng, Z.-E. Su, Y. Hu, Y.-M. He, X. Ding, W. Zhang, H. Li, L. Zhang, Z. Wang, L. You, X.-L. Wang, X. Jiang, L. Li, Y.-A. Chen, N.-L. Liu, C.-Y. Lu, and J.-W. Pan, "12-photon entanglement and scalable scattershot boson sampling with optimal entangled-photon pairs from parametric down-conversion," Phys. Rev. Lett. **121**, 250505 (2018).
22. J.-W. Wang, F. Sciarrino, A. Laing, and M. G. Thompson, "Integrated photonic quantum technologies," Nat. Photonics **14**, 273–284 (2020).
23. F. Flamini, N. Spagnolo, and F. Sciarrino, "Photonic quantum information processing: a review," Rep. Prog. Phys. **82**, 016001 (2019).
24. J. B. Spring, P. S. Salter, B. J. Metcalf, P. C. Humphreys, M. Moore, N. Thomas-Peter, M. Barbieri, X.-M. Jin, N. K. Langford, W. S. Kolthammer, M. J. Booth, and I. A. Walmsley, "On-chip low loss heralded source of pure single photons," Opt. Express **21**, 13522–13532 (2013).
25. J. B. Spring, P. L. Mennea, B. J. Metcalf, P. C. Humphreys, J. C. Gates, H. L. Rogers, C. Söller, B. J. Smith, W. S. Kolthammer, P. G. R. Smith, and I. A. Walmsley, "A chip-based array of near-identical, pure, heralded single photon sources," Optica **4**, 90–96 (2017).
26. J. W. Silverstone, D. Bonneau, K. Ohira, N. Suzuki, H. Yoshida, N. Iizuka, M. Ezaki, C. M. Natarajan, M. G. Tanner, R. H. Hadfield, V. Zwiller, G. D. Marshall, J. G. Rarity, J. L. O'Brien, and M. G. Thompson, "On-chip quantum interference between silicon photon-pair sources," Nat. Photonics **8**, 104–108 (2014).
27. S. Paesani, M. Borghi, S. Signorini, A. Maïnos, L. Pavesi, and A. Laing, "Near-ideal spontaneous photon sources in silicon quantum photonics," Nat. Commun. **11**, 2505 (2020).
28. R.-J. Ren, J. Gao, W.-H. Zhou, Z.-Q. Jiao, L.-F. Qiao, X.-W. Wang, and X.-M. Jin, "128 identical quantum sources integrated on a single silica chip," Phys. Rev. Applied **16**, 054026 (2021).
29. J.-W. Wang, S. Paesani, Y. Ding, R. Santagati, P. Skrzypczyk, A. Salavrakos, J. Tura, R. Augusiak, L. Mančinska, D. Bacco, D. Bonneau, J. W. Silverstone, Q. Gong, A. Acín, K. Rottwitt, L. K. Oxenløwe, J. L. O'Brien, A. Laing, and M. G. Thompson, "Multidimensional quantum entanglement with large-scale integrated optics," Science **360**, 285–291 (2018).
30. K. M. Davis, K. Miura, N. Sugimoto, and K. Hirao, "Writing waveguides in glass with a femtosecond laser," Opt. Lett. **21**, 1729–1731 (1996).
31. R. Osellame, G. Cerullo, and R. Ramponi, *Femtosecond Laser Micromachining: Photonic and Microfluidic Devices in Transparent Materials* (Springer, 2012).
32. H. Tang, X.-F. Lin, Z. Feng, J.-Y. Chen, J. Gao, K. Sun, C.-Y. Wang, P.-C. Lai, X.-Y. Xu, Y. Wang, L.-F. Qiao, A.-L. Yang, and X.-M. Jin, "Experimental two-dimensional quantum walk on a photonic chip," Sci. Adv. **4**, eaat3174 (2018).
33. H. Tang, C. D. Franco, Z.-Y. Shi, T.-S. He, Z. Feng, J. Gao, K. Sun, Z.-M. Li, Z.-Q. Jiao, T.-Y. Wang, M. S. Kim, and X.-M. Jin, "Experimental quantum fast hitting on hexagonal graphs," Nat. Photonics **12**, 754–758 (2018).
34. Z.-Q. Jiao, J. Gao, W.-H. Zhou, X.-W. Wang, R.-J. Ren, X.-Y. Xu, L.-F. Qiao, Y. Wang, and X.-M. Jin, "Two-dimensional quantum walk of correlated photons," Optica **8**, 1129–1135 (2021).
35. D. Leykam, A. S. Solntsev, A. A. Sukhorukov, and A. S. Desyatnikov, "Lattice topology and spontaneous parametric down-conversion in quadratic nonlinear waveguide arrays," Phys. Rev. A **92**, 033815 (2015).
36. D. Smirnova, D. Leykam, Y. Chong, and Y. Kivshar, "Nonlinear topological photonics," Appl. Phys. Rev. **7**, 021306 (2020).
37. A. Blanco-Redondo, B. Bell, D. Oren, B. J. Eggleton, and M. Segev, "Topological protection of biphoton states," Science **362**, 568–571 (2018).
38. M. Wang, C. Doyle, B. Bell, M. J. Collins, E. Magi, B. J. Eggleton, M. Segev, and A. Blanco-Redondo, "Topologically protected entangled photonic states," Nanophotonics **8**, 1327–1335 (2019).
39. K. Tschernig, Á. Jimenez-Galán, D. N. Christodoulides, M. Ivanov, K. Busch, M. A. Bandres, and A. Perez-Leija, "Topological protection versus degree of entanglement of two-photon light in photonic topological insulators," Nat. Commun. **12**, 1974 (2021).
40. M. C. Rechtsman, Y. Lumer, Y. Plotnik, A. Perez-Leija, A. Szameit, and M. Segev, "Topological protection of photonic path entanglement," Optica **3**, 925–930 (2016).
41. Y. Wang, X.-L. Pang, Y.-H. Lu, J. Gao, Y.-J. Chang, L.-F. Qiao, Z.-Q. Jiao, H. Tang, and X.-M. Jin, "Topological protection of two-photon quantum correlation on a photonic chip," Optica **6**, 955–960 (2019).
42. Y. Wang, Y.-H. Lu, J. Gao, R.-J. Ren, Y.-J. Chang, Z.-Q. Jiao, Z.-Y. Zhang, and X.-M. Jin, "Topologically protected quantum entanglement," arXiv:1903.03015 (2019).
43. W. P. Su, J. R. Schrieffer, and A. J. Heeger, "Solitons in polyacetylene," Phys. Rev. Lett. **42**, 1698–1701 (1979).
44. L. Lu, J. D. Joannopoulos, and M. Soljacic, "Topological photonics," Nat. Photonics **8**, 821–829 (2014).
45. T. Ozawa, H. M. Price, A. Amo, N. Goldman, M. Hafezi, L. Lu, M. C. Rechtsman, D. Schuster, J. Simon, O. Zilberberg, and I. Carusotto, "Topological photonics," Rev. Mod. Phys. **91**, 015006 (2019).
46. A. Blanco-Redondo, I. Andonegui, M. J. Collins, G. Harari, Y. Lumer, M. C. Rechtsman, B. J. Eggleton, and M. Segev, "Topological optical waveguiding in silicon and the transition between topological and trivial defect states," Phys. Rev. Lett. **116**, 163901 (2016).
47. J. Zak, "Berry's phase for energy bands in solids," Phys. Rev. Lett. **62**, 2747–2750 (1989).
48. P. Delplace, D. Ullmo, and G. Montambaux, "Zak phase and the existence of edge states in graphene," Phys. Rev. B **84**, 195452 (2011).
49. J. Noh, W. A. Benalcazar, S. Huang, M. J. Collins, K. P. Chen, T. L. Hughes, and M. C. Rechtsman, "Topological protection of photonic mid-gap defect modes," Nat. Photonics **12**, 408–415 (2018).
50. A. Moroz, "Minima and maxima of the local density of states for one-dimensional periodic systems," Europhys. Lett. **46**, 419–424 (1999).
51. M. Verbin, O. Zilberberg, Y. E. Kraus, Y. Lahini, and Y. Silberberg, "Observation of topological phase transitions in photonic quasicrystals," Phys. Rev. Lett. **110**, 076403 (2013).
52. H. de Riedmatten, J. Laurat, C. W. Chou, E. W. Schomburg, D. Felinto, and H. J. Kimble, "Direct measurement of decoherence for entanglement between a photon and stored atomic excitation," Phys. Rev. Lett. **97**, 113603 (2006).
53. A. Christ, K. Laiho, A. Eckstein, K. N. Cassemiro, and C. Silberhorn, "Probing multimode squeezing with correlation functions," New J. Phys. **13**, 033027 (2011).
54. A. I. Lvovsky, "Squeezed light," in *Photonics*, D. L. Andrews, ed. (Wiley, 2015), Chapter 5.
55. J. M. Arrazola, V. Bergholm, K. Brádler, T. R. Bromley, M. J. Collins, I. Dhand, A. Fumagalli, T. Gerrits, A. Goussev, L. G. Helt, J. Hundal, T. Isacsson, R. B. Israel, J. Izaac, S. Jahangiri, R. Janik, N. Killoran, S. P. Kumar, J. Lavoie, A. E. Lita, D. H. Mahler, M. Menotti, B. Morrison, S. W. Nam, L. Neuhaus, H. Y. Qi, N. Quesada, A. Repingon, K. K. Sabapathy, M. Schuld, D. Su, J. Swinarton, A. Száva, K. Tan, P. Tan, V. D. Vaidya, Z. Vernon, Z. Zabaneh, and Y. Zhang, "Quantum circuits with many photons on a programmable nanophotonic chip," Nature **591**, 54–60 (2021).
56. A. Szameit, F. Dreisow, T. Pertsch, S. Nolte, and A. Tünnermann, "Control of directional evanescent coupling in fs laser written waveguides," Opt. Express **15**, 1579–1587 (2007).